JOURNAL OF MATERIALS SCIENCE 29 (1994) 816–823

Crystallization of amorphous $Fe_{78}B_{13}Si_9$

A. R. BHATTI*, B. CANTOR
Oxford Centre for Advanced Materials and Composites, Department of Materials, University of Oxford, Parks Road, Oxford OX1 3PH, UK

Crystallization of amorphous $Fe_{78}B_{13}Si_9$ has been investigated using a combination of differential scanning calorimetry (DSC) and conventional and high-resolution transmission electron microscopy. The crystallization mechanisms and crystalline products are sensitive to the annealing temperature. At 450 °C, crystallization takes place by the growth of bcc α-Fe (Si) dendrites, while at 510 and 515 °C there are three simultaneous reactions to form dendritic bcc α-Fe (Si), elliptical crystals of bct Fe_3B and lamellar eutectic spherulites of bcc α-Fe (Si) and bct Fe_3B. Quantitative TEM shows that the bcc α-Fe (Si) dendrites and bcc α-Fe (Si)–bct Fe_3B spherulites both form with constant nucleation and growth rates, in agreement with previous DSC measurements of an Avrami exponent of 4.

1. Introduction

Amorphous alloys exhibit a variety of desirable electrical, magnetic, chemical and mechanical properties which are different from those of conventional crystalline alloys [1–5]. Soft ferromagnetic iron-based amorphous alloys, such as $Fe_{78}B_{13}Si_9$, are of particular technological importance as core materials in distribution transformers. In applications such as distribution transformer cores, amorphous alloys must operate for long periods of time at moderate service temperatures. However, amorphous alloys are inherently unstable and prone to crystallization during thermal exposure, leading to degradation of the special alloy properties and component failure during service [6, 7]. Successful exploitation of amorphous alloys depends critically, therefore, on understanding and controlling their crystallization behaviour during heat treatment.

There has not previously been any systematic detailed investigation of the crystallization behaviour of amorphous $Fe_{78}B_{13}Si_9$, except for differential scanning calorimetry (DSC) studies by Hughes *et al.* [8]. The amorphous alloy was found to exhibit a double exothermic crystallization peak. Johnson–Mehl–Avrani (JMA) analysis of isothermal DSC traces and Kissinger analysis of continuous DSC traces showed an Avrami exponent of 4.0 and activation energies for crystallization of 404 and 385 $KJ\,mol^{-1}$, respectively.

This paper describes the results of a detailed investigation of the microstructure and kinetics of crystallization in amorphous $Fe_{78}B_{13}Si_9$, using a combination of DSC, conventional transmission electron microscopy (TEM) and high-resolution transmission electron microscopy (HREM).

2. Experimental procedure

The amorphous $Fe_{78}B_{13}Si_9$ alloy (kindly supplied by Dr A. Taub, General Electric), was in the form of a long ribbon with a cross-section typically 30 μm × 25 mm. Alloy samples were heat treated isothermally under a dynamic argon atmosphere in a Dupont 1090 thermal analyser/910 DSC, at annealing temperatures in the range 450–515 °C for annealing times ranging from 3–30 min. The heat treatments were selected using the previous isothermal annealing DSC curves obtained by Hughes *et al.* [8].

Thin-foil specimens for TEM and HREM were produced using a twin-gun Gatan ion-beam miller operating at 4 keV, 0.5 mA and a grazing angle of 15 °, with continual specimen rotation to ensure perforation in the foil centre. The resulting thin-foil specimens were examined in a Jeol 100C TEM and a Jeol 200C HREM.

3. Results and discussion

3.1. Crystal microstructure

Fig. 1 shows a typical DSC trace exhibiting a double-peaked exotherm, obtained during isothermal crystallization of amorphous $Fe_{78}B_{13}Si_9$ at 510 °C. TEM examination of thin foils for various times at 510 °C showed that the amorphous structure was essentially unchanged until crystallization began after 6 min. Three different kinds of crystal appeared to form simultaneously from the very earliest stages of crystallization, and crystallization was complete after the end of the first peak.

Fig. 2 shows a typical transmission electron micrograph of the three kinds of co-existing crystals obtained after heat treatment for 13 min at 510 °C. The first kind of crystal, marked 1 in Fig. 2, was star-shaped or dendritic with two-fold, three-fold or four-fold symmetry, similar to the morphology reported by Schwartz *et al.* [9]. Fig. 3 shows a higher magnification image of a dendritic crystal, and Fig. 4 shows a typical selected-area diffraction pattern, superimposed

---

* *Present address*: Department of Materials and Structures, DRA Farnborough, Hampshire GU14 6TD, UK.

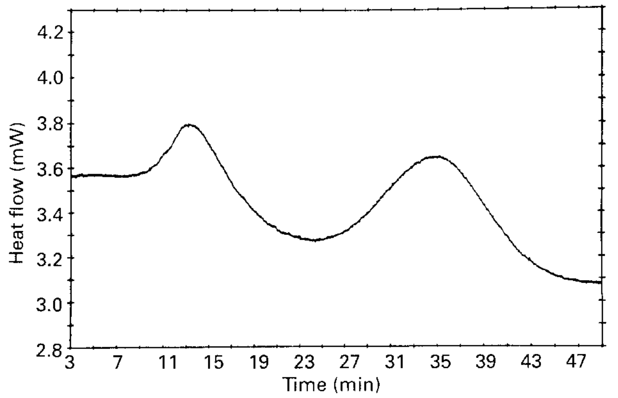

Figure 1 Crystallization exotherms during isothermal heating of amorphous $Fe_{78}B_{13}Si_9$ at 510 °C.

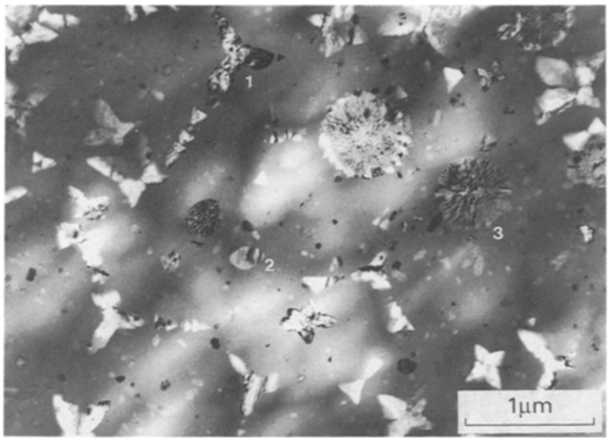

Figure 2 Bright-field transmission electron micrograph of amorphous $Fe_{78}B_{13}Si_9$ after 13 min at 510 °C, showing formation of (1) dendritic crystals of b c c α-Fe, (2) elliptical crystals of b c t Fe_3B, and (3) lamellar spherulites of b c c α-Fe and b c t Fe_3B.

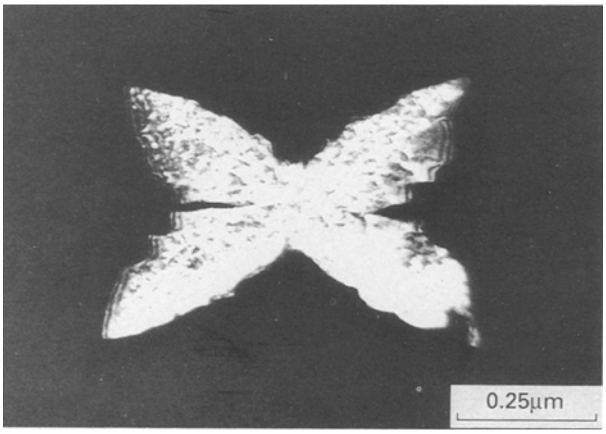

Figure 3 Bright-field transmission electron micrograph of amorphous $Fe_{78}B_{13}Si_9$ after 13 min at 510 °C, showing dendritic crystal at high magnification.

on the corresponding dendritic crystal, which was indexed as b c c α-Fe with lattice parameter $a = 0.28664$ nm. Extra superlattice spots were occasionally observed, as shown in Fig. 5, which were indexed as DO_3 ordered Fe_3Si with lattice parameter $a = 0.564$ nm. The dendrite arm direction was [1 1 0] and the truncated dendritic faces were close to (1 0 0). Fig. 6 shows a high-resolution electron micrograph of

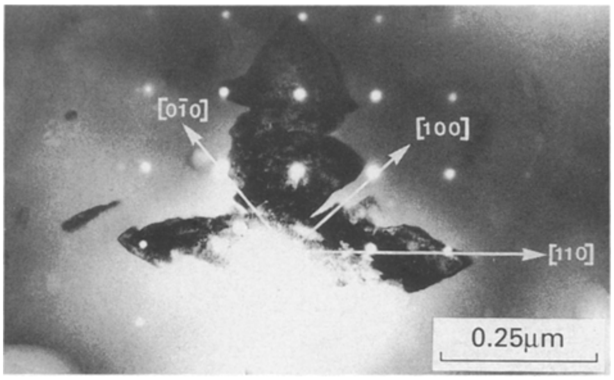

Figure 4 Bright-field transmission electron micrograph of amorphous $Fe_{78}B_{13}Si_9$ after 13 min at 510 °C, showing a dendritic crystal and corresponding selected-area electron diffraction pattern (superimposed).

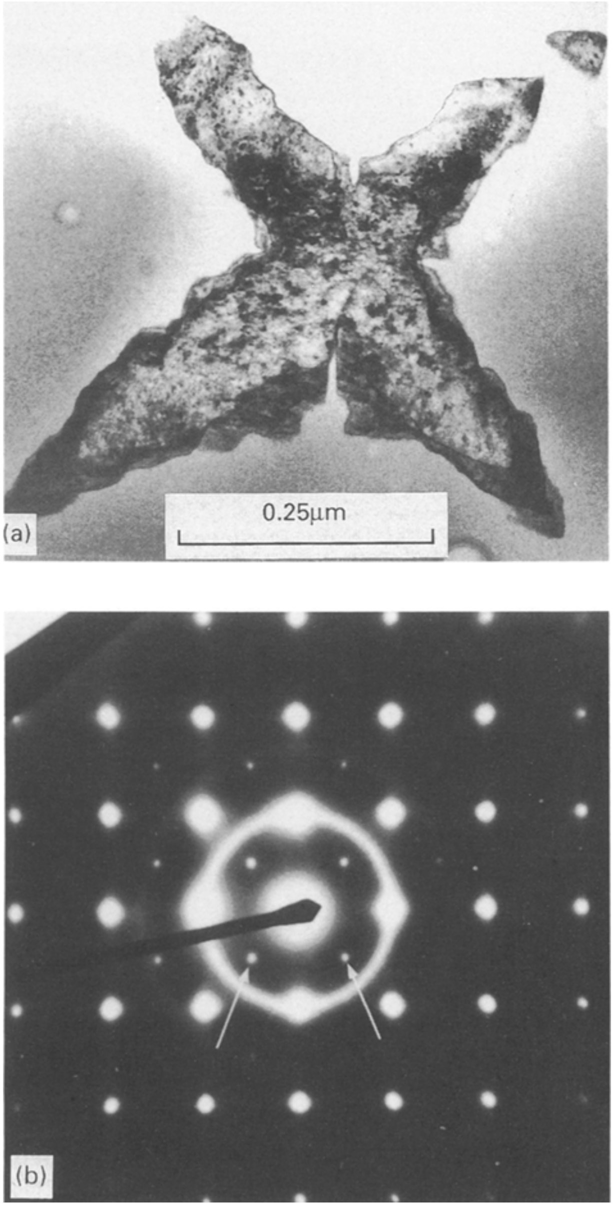

Figure 5 (a,b) Bright-field transmission electron micrograph of amorphous $Fe_{78}B_{13}Si_9$ after 13 min at 510 °C, showing a dendritic crystal and corresponding selected-area electron diffraction pattern with extra spots (arrowed) which correspond to DO_3 ordered Fe_3Si.

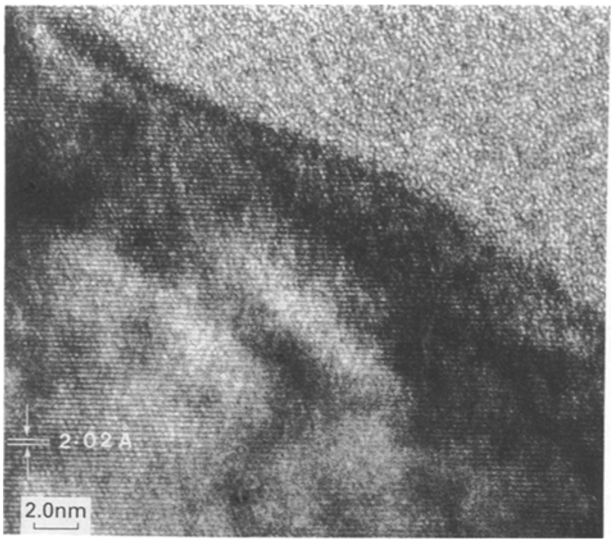

Figure 6 High-resolution electron micrograph of amorphous $Fe_{78}B_{13}Si_9$ after 13 min at 510 °C, showing (1 1 0) planes of interface between dendritic b c c α-Fe crystal and amorphous matrix.

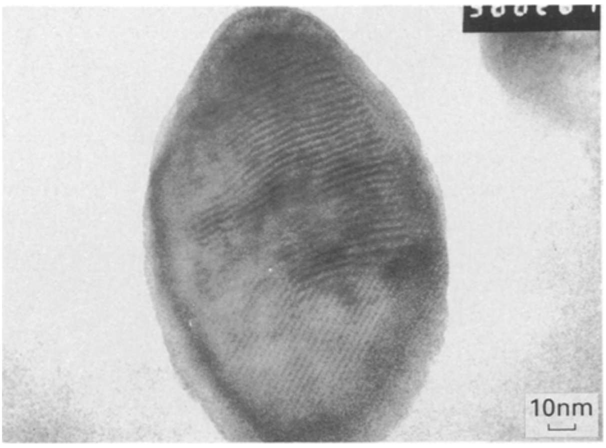

Figure 7 High-resolution electron micrograph of amorphous $Fe_{78}B_{13}Si_9$ after 13 min at 510 °C, showing an elliptical crystal at high magnification.

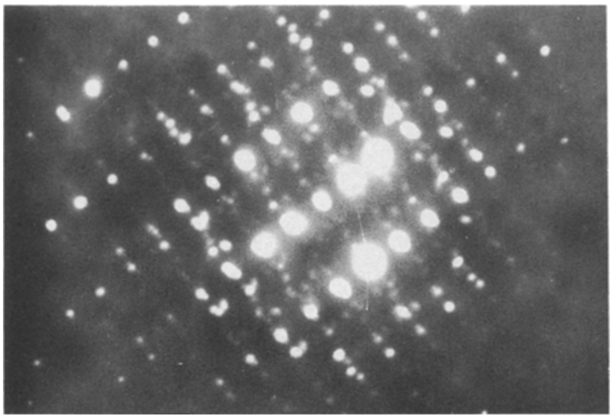

Figure 8 Selected-area electron diffraction pattern corresponding to the elliptical crystal in Fig. 7.

(1 1 0) lattice fringes at the interface between a dendritic α-Fe crystal and the amorphous matrix. The interface was diffuse and not bounded by sharply defined facets.

The second kind of crystal, marked 2 in Fig. 2, was approximately elliptical in shape. Fig. 7 shows a higher magnifaction image of an elliptical-shaped crystal, and Fig. 8 shows the corresponding selected-area diffraction pattern, which was indexed as b c t Fe_3B with lattice parameters $a = 0.862$ nm and

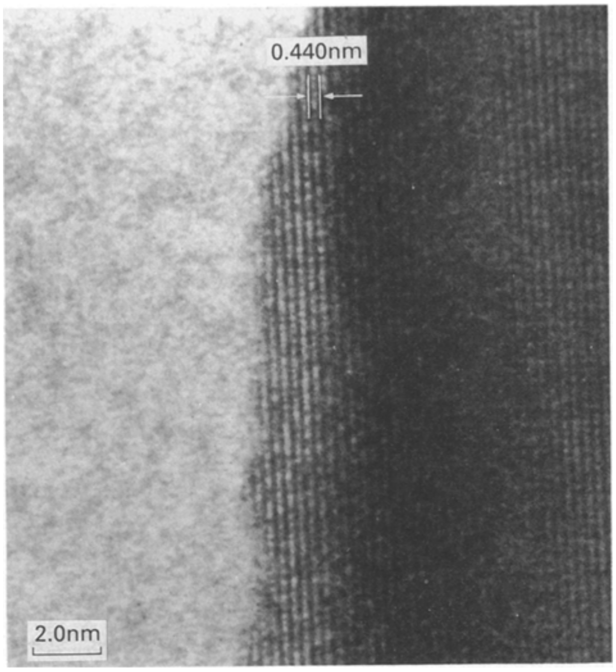

Figure 9 High-resolution electron micrograph of amorphous $Fe_{78}B_{13}Si_9$ after 13 min at 510 °C, showing interface between elliptical b c t Fe_3B crystal and amorphous matrix.

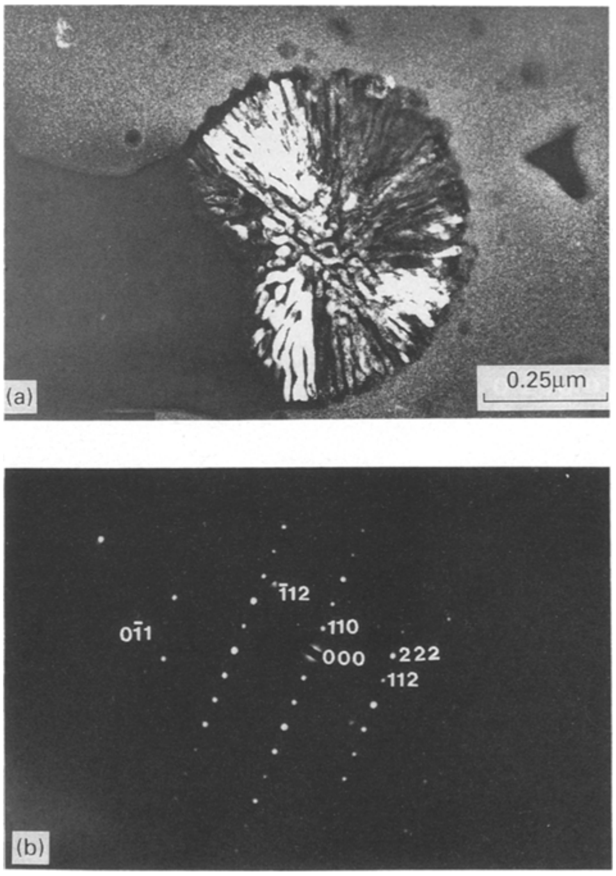

Figure 10 (a) Dark-field transmission electron micrograph of amorphous $Fe_{78}B_{13}Si_9$ after 13 min at 510 °C, showing spherulites with lamellar structure. (b) Selected-area electron diffraction pattern from (a) showing lamellar b c c α-Fe and b c t Fe_3B phases.

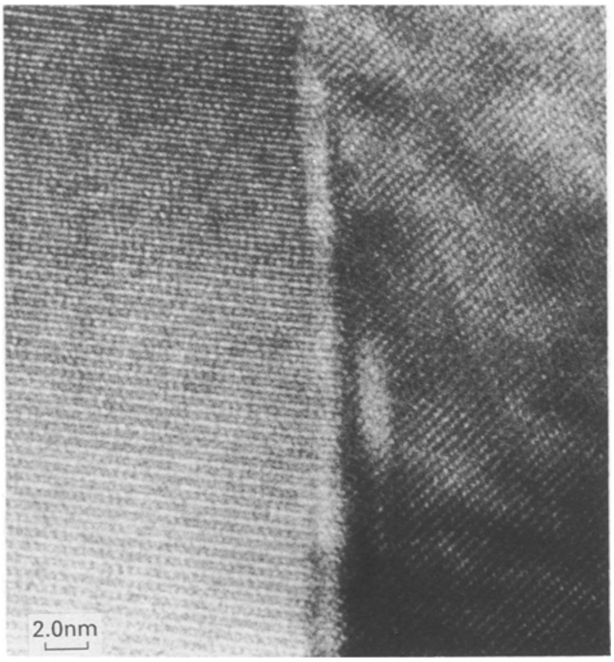

Figure 11 High-resolution micrograph of amorphous $Fe_{78}B_{13}Si_9$ after 13 min at 510 °C showing (1 1 0) b c c α-Fe and (2 0 0) b c t Fe_3B phases at spherulitic lamellar interface.

$c = 0.429$ nm. Fig. 9 shows a high-resolution electron micrograph of (2 0 0) lattice fringes at the interface between an Fe_3B elliptical crystal and the amorphous matrix. The Fe_3B interface was sharper than the α-Fe interface shown in Fig. 6, with some evidence of interface steps. This suggests that crystal growth may take place by a lateral step migration mechanism.

The third kind of crystal, marked 3 in Fig. 2, was spherulitic in shape, with a radial structure. Detailed analysis of selected-area electron diffraction patterns and dark-field images such as in Fig. 10, revealed that each spherulite consisted of two interpenetrating single crystals of b c c α-Fe and b c t Fe_3B. Crystals similar in size to the elliptical Fe_3B crystals were sometimes found in the core of a spherulite, indicating that they were precursor nuclei for spherulitic growth. Fig. 12a–c show spherulites at different stages of growth, with a central Fe_3B nucleus in dark contrast marked A, and an outer α-Fe region in light contrast marked B.

With decreasing annealing temperature, there was a gradual change in crystallization morphology. The extent of spherulitic crystallization decreased, and the extent of dendritic crystallization increased. Fig. 13 shows an example of this in a sample partially crystallized for 30 min at 450 °C, which crystallized almost completely to b c c α-Fe dendrites.

In summary, amorphous $Fe_{78}B_{13}Si_9$, crystallizes in a complex way, with the crystallization mechanism dependent on the annealing temperature. At low temperatures such as 450 °C, crystallization takes place by the growth of b c c α-Fe. At intermediate temperatures such as 510 °C, there are three simultaneous reactions to form dendritic b c c α-Fe, elliptical nodules of b c t Fe_3B and lamellar eutectic spherulites of b c c α-Fe and b c t Fe_3B. The dendritic and spherulitic b c c α-Fe incorporates some silicon in solid solution, sometimes leading to the formation of DO_3 ordered Fe_3Si. The elliptical Fe_3B nodules act as nuclei for subsequent growth of the lamellar eutectic spherulites. The small Fe_3B nodules form first, enriching the surrounding matrix in iron, and promoting secondary nucleation of α-Fe. The two adjacent crystals of α-Fe and Fe_3B, then grow co-operatively with a lamellar eutectic spherulitic structure. Similar eutectic spherulites of f c c Fe (Ni) and b c t (Fe, Ni)$_3$ (B, P) have been previously reported to form in partially crystallized

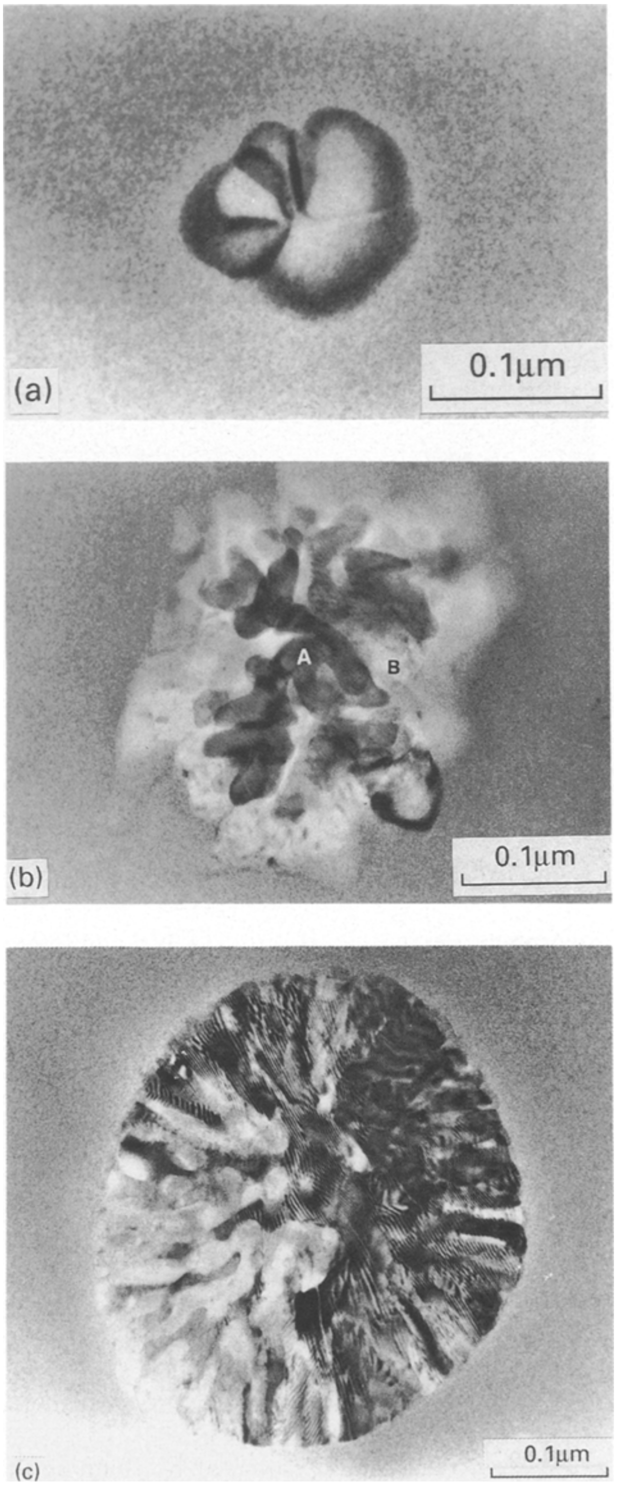

Figure 12 Bright-field transmission electron micrographs showing spherulites at different stages of growth in amorphous $Fe_{78}B_{13}Si_9$ after heat treatment at 515 °C for (a) 3 min, (b) 5 min, and (c) 10 min.

Figure 13 Bright-field transmission electron micrograph of amorphous $Fe_{78}B_{13}Si_9$ after 30 min at 450 °C.

amorphous $Fe_{40}Ni_{40}P_{14}B_6$ [10, 11]. Wei and Cantor [12] have reported that crystallization of amorphous $Fe_{78}B_{13}Si_9$, at even higher temperatures such as 600 °C, results in a different multiphase structure, consisting of a mixture of α-Fe, Fe_2B and Fe_3Si.

3.2. Nucleation and growth kinetics

Crystal nucleation and growth rates were measured at two different temperatures: 510 and 515 °C, Fig. 14a–d show the sequence of isothermal transformation at 510 °C after 6,8,13 and 23 min, respectively, and similarly Fig. 15a–c show the sequence of isothermal transformation at 515 °C after 3,5 and 10 min, respectively. Figs 14 and 15 indicate clearly how new crystals were continually nucleated at the same time as the existing ones increased in size.

Nucleation rates were estimated by counting the number of crystals per unit area, N_A, and then calculating the number of crystals per unit volume, N_v, from the relation $N_v = N_A/(D + X)$ [13], where D is the average size of each crystal and X is the specimen thickness. N_A and D were measured directly from transmission electron micrographs such as in Figs 14 and 15, and X was taken as 100 nm with an accuracy of ± 10%. The resulting estimates of nucleation density for dendritic and spherulitic crystals at both 510 and 515 °C are presented in Tables I and II and Figs 16 and 17. The results in Tables I and II and Figs 16 and 17 are average values from several transmission electron micrographs. For each type of crystal at each temperature, the nucleation density increased linearly with time, i.e. there was a constant nucleation rate, dN_v/dt.

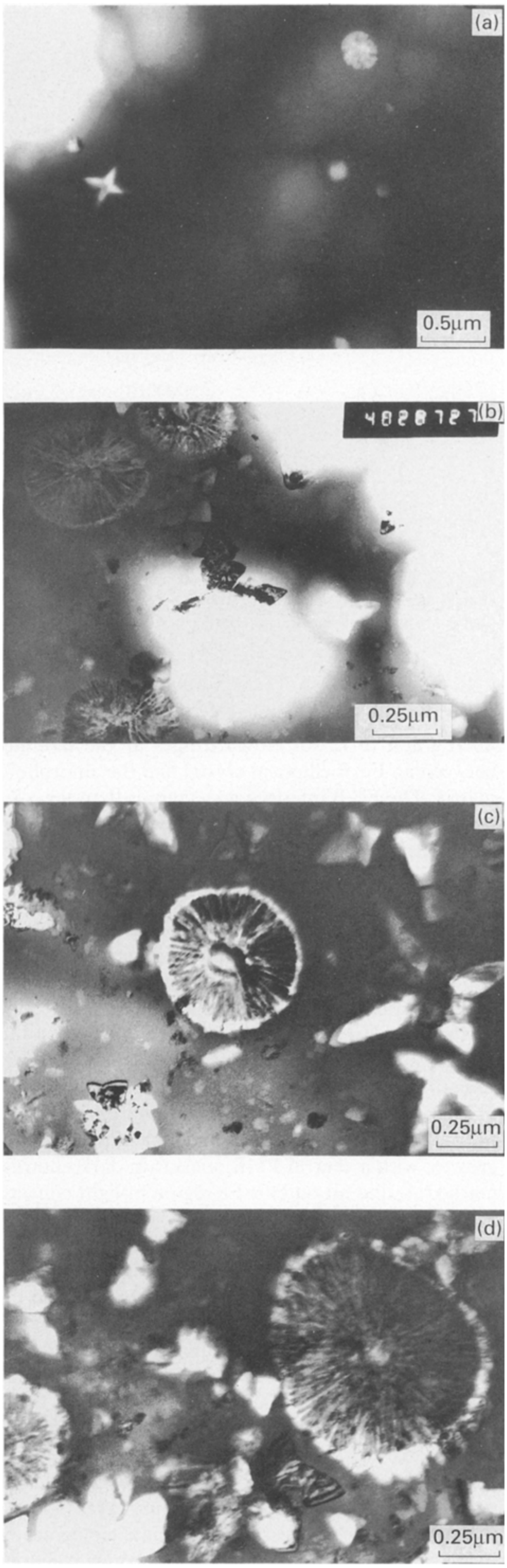

Figure 14 Bright-field transmission electron micrographs of isothermal crystallization of amorphous $Fe_{78}B_{13}Si_9$ at 510 °C after (a) 6 min, (b) 8 min, (c) 13 min, and (d) 23 min.

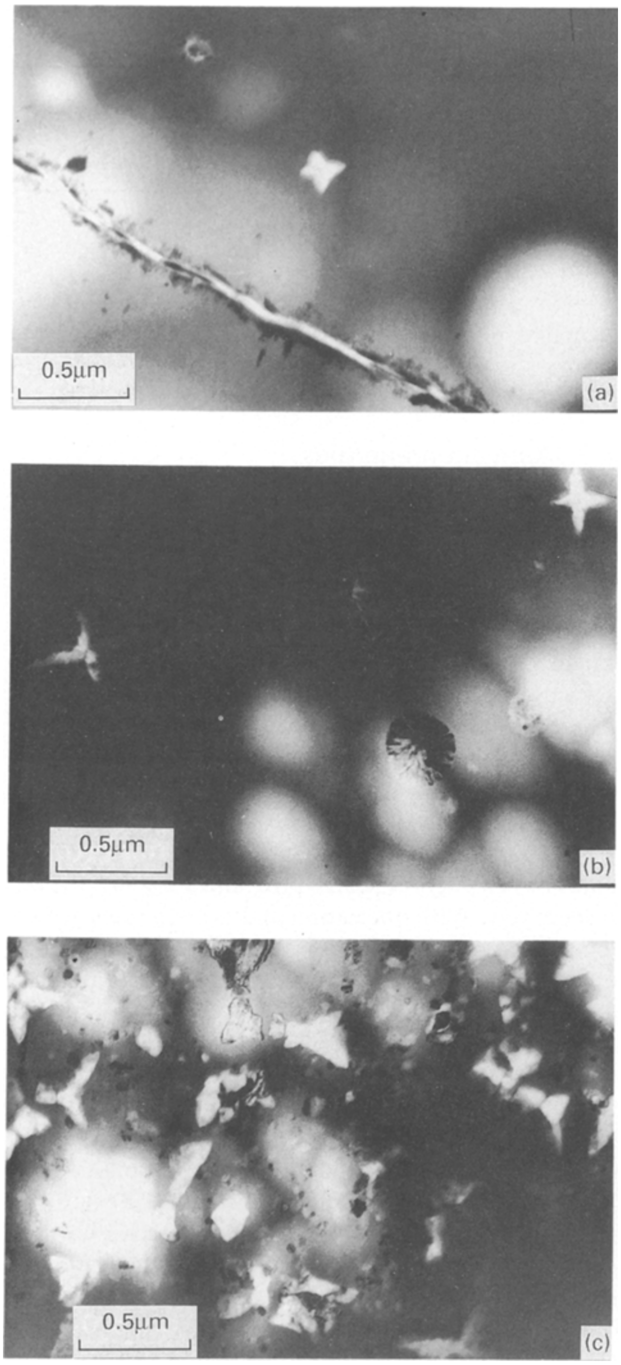

Figure 15 Bright-field transmission electron micrographs of isothermal crystallization of amorphous $Fe_{78}B_{13}Si_9$ at 515 °C after (a) 3 min, (b) 5 min, and (c) 10 min.

Crystal growth rates dD_{max}/dt were estimated directly by measuring the variations of maximum crystal size with annealing time, assuming the largest crystal nucleated immediately. Dendrite arm length and radius were used to measure dendrite and spherulite crystal size, respectively, at both 510 and 515 °C. The resulting estimates of crystal growth rate are presented in Table III and Figs 18 and 19, as average values from several transmission electron micrographs. The growth rates were similar for the two types of crystal, as expected because they grew almost simultaneously.

The number density of each type of crystal increased linearly with increasing annealing time, corresponding to a crystal nucleation rates in the range 0.03–0.63 $\mu m^3 min^{-1}$. The maximum size of each type

TABLE I Particle density after isothermal annealing at 510 °C

Annealing time (min)	Number of crystals per unit volume N_v (μm^{-3})	
	Dendritic	Spherulitic
6	0.60	0.21
8	2.0	0.31
13	5.0	0.50

TABLE II Particle density after isothermal annealing at 515 °C

Annealing time (min)	Number of crystals per unit volume, N_v (μm^{-3})	
	Dendritic	Spherulitic
3	0.31	0.35
5	1.7	0.47
10	6.3	0.71

TABLE III Growth rates for dendritic and spherulitic crystals

Isothermal annealing temp. (°C)	Growth rates, dD_{max}/dt (nm min^{-1})	
	Dendritic	Spherulitic
510	27	21
515	35	25

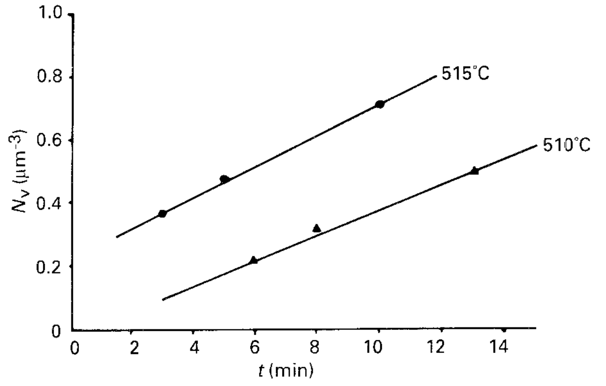

Figure 16 Number of spherulitic crystals per unit volume, N_v, versus time, t, for amorphous $Fe_{78}B_{13}Si_9$ annealed at 510° and 515 °C.

of crystal also increased linearly with increasing annealing time, corresponding to crystal growth rates in the range 21–35 nm min^{-1}. These quantative TEM kinetic results appear to be consistent with previous DSC kinetic results for amorphous $Fe_{78}B_{13}Si_9$ [8] with an isothermal Avrami exponent of 4, corresponding to constant nucleation rate and linear three-dimensional growth. However, the results do not agree with Chang and Marti's [14] observation of parabolic dendritic growth in amorphous $Fe_{78}B_{12}Si_8$.

The failure of the growth rate data to pass through zero in Figs 18 and 19 may be attributed to the time

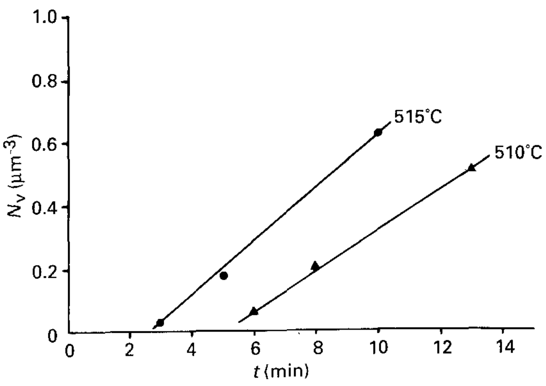

Figure 17 Number of dendritic crystals per unit volume, N_v, versus time, t, for amorphous $Fe_{78}B_{13}Si_9$ annealed at 510° and 515 °C.

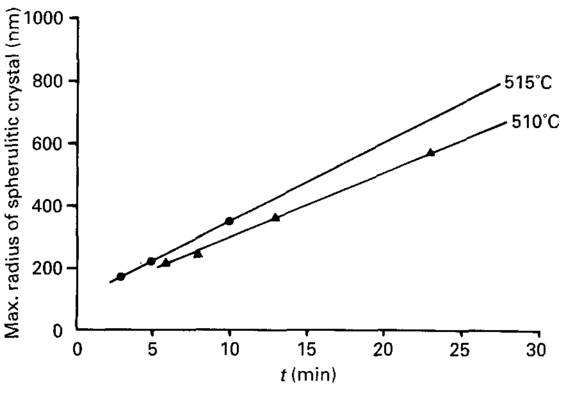

Figure 18 Maximum radius of spherulitic crystals, D_{max}, versus annealing time, t, for amorphous $Fe_{78}B_{13}Si_9$ annealed at 510° and 515 °C.

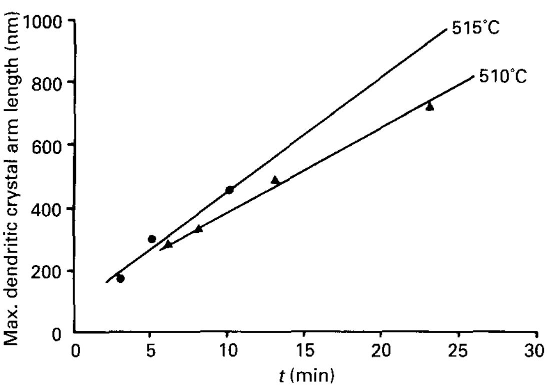

Figure 19 Maximum dendritic crystal arm length, D_{max}, versus annealing time, t, for amorphous $Fe_{78}B_{13}Si_9$ annealed at 510° and 515 °C.

required to reach the working temperature in the annealing furnace. This warm-up time was equivalent to ~ 3.5 min at the annealing temperature, estimated from Figs 18 and 19 by extrapolating back to zero. Similarly, positive intercepts on the time axis for the nucleation rate data in Figs 16 and 17 may be associated with a transient period before steady-state nucleation takes place. However, it is then difficult to understand the apparent crystal growth at earlier times. An alternative explanation is that crystal growth is initially fast, and then stabilizes at the growth rates shown in Figs 18 and 19.

TABLE IV Activation energies for crystal nucleation, Q_n, and growth, Q_g, in amorphous $Fe_{78}B_{13}Si_9$

Type of crystal	Q_n (kJ mol^{-1})	Q_g (kJ mol^{-1})
Dendritic	299	270
Spherulitic	260	187

3.3. Activation energies

The nucleation and growth rates, dN_v/dt and dD_{max}/dt, can both be expressed in Arrhenius form

$$dN_v/dt = N_0 \exp(-Q_n/RT) \quad (1)$$

$$dD_{max}/dt = D_0 \exp(-Q_g/RT) \quad (2)$$

where Q_n and Q_g are the nucleation and growth activation energies, R is the gas constant and N_0 and D_0 are constants. The measured crystal nucleation and growth rates were inserted in Equations 1 and 2 to calculate the nucleation and growth activation energies Q_n and Q_g, as described previously by Von Heimendahl and Kuglstatter [15] and Tiwari *et al.* [16] for amorphous $Fe_{32}Ni_{36}Cr_{14}P_{12}B_6$ and $Fe_{40}Ni_{40}P_{14}B_6$, respectively. With nucleation and growth rates at two temperatures only 5 °C apart, the measured nucleation and growth activation energies are only accurate to ± 25%.

The resulting activation energies for nucleation of spherulites and dendrites were 260 and 299 kJ mol^{-1}, respectively. The activation energy for growth of spherulites was 187 kJ mol^{-1}, in reasonable agreement with the value of 174 kJ mol^{-1}, obtained by Koster and Herold [17] for growth of α-Fe + Fe_3B spherulites in $Fe_{80}B_{20}$. However, the activation energy for growth of dendrites was 271 kJ mol^{-1}, significantly different from the value of 154 kJ mol^{-1} obtained by Chang and Marti [14] for growth of α-(Fe, Si) dendrite crystals in amorphous $Fe_{80}Si_{12}B_8$. Table IV lists the measured activation energies for nucleation and growth of dendritic and spherulitic crystals in amorphous $Fe_{78}B_{13}Si_9$.

4. Conclusions

Amorphous $Fe_{78}B_{13}Si_9$ crystallizes in a complex way, with crystallization mechanisms and crystalline products which are sensitive to the annealing temperature. At 450 °C, crystallization takes place by the growth of bcc α-Fe (Si) dendrites, while at 510 and 515 °C there are three simultaneous reactions to form dendritic bcc α-Fe (Si), elliptical crystals of bct Fe_3B and lamellar eutectic spherulites of bcc α-Fe (Si) bct Fe_3B. Quantitative TEM shows that the bcc α-Fe (Si) dendrites and the lamellar eutectic bcc α-Fe (Si)–Fe_3B spherulites both form with constant nucleation and growth rates, in agreement with previous DSC measurements of an Avrami exponent of 4. The complex crystallization microstructure in amorphous $Fe_{78}B_{13}Si_9$ indicates that it may be difficult to extrapolate DSC kinetic results to calculate operating lifetimes at technological working temperatures without detailed supporting transmission electron microscopy.

References

1. B. CANTOR (ed.), "Rapidly Quenched Metals III" (Metals Society, 1978).
2. T. MASUMOTO and K. SUZUKI (eds), "Rapidly Quenched Metals IV" (Japan Institute of Metals, 1982).
3. H. WARLIMONT and S. STEEB (eds), "Rapidly Quenched Metals V" (North Holland, 1985).
4. H. HERMAN (ed.), "Rapidly Quenched Metals VI" (Elsevier, 1988).
5. H. FREDERIKSSON and S. SAVAGE (eds), "Rapidly Quenched Materials VIII" (Elsevier, 1991).
6. M. G. SCOTT, in "Amorphous Metallic Alloys", edited by F. E. Luborsky (Butterworths, 1983) p. 144.
7. A. R. BHATTI, J. C. BARRY and B. CANTOR, *Proc. Mater. Res. Soc.* **58** (1986) 99.
8. M. A. HUGHES, A. R. BHATTI, G. WEI and B. CANTOR, *Mater. Forum* **11** (1988) 21.
9. J. C. SCHWARTZ, R. KOSSOWSKY, J. J. HUGHES and R. F. KRAUSE, *J. Appl. Phys.* **52** (1981) 3324.
10. T. WATNABE and M. G. SCOTT, *J. Mater. Sci.* **15** (1980) 1131.
11. U. KOSTER and U. HEROLD, in "Glassy Metals 1", edited by H. J. Guntherodt and H. Beck (Springer, Berlin, 1982) p. 225.
12. G. WEI and B. CANTOR, *Acta Metall.* **36** (1988) 2293.
13. J. A. BELK and A. L. DAVIES (eds), "Electron Microscopy and Microanalysis of Metals" (Elsevier, Amsterdam, 1965) p. 96.
14. C. F. CHANG and J. MARTI, *J. Mater. Sci.* **18** (1983) 2297.
15. M. VON HEIMENDAHL and G. KUGLSTATTER, *ibid.* **16** (1981) 2405.
16. R. S. TIWARI, S. RANGANATHAN and M. VON HEIMENDAHL, *Z. Metallkde* **8** (1981) 563.
17. U. KOSTER and U. HEROLD, *Scripta Metall.* **12** (1978) 75.

Received 18 March 1993
and accepted 8 June 1993